Article

Research on Control Strategies of an Open-End Winding Permanent Magnet Synchronous Driving Motor (OW-PMSM)-Equipped Dual Inverter with a Switchable Winding Mode for Electric Vehicles

Liang Chu [1], Yi-fan Jia [1], Dong-sheng Chen [1], Nan Xu [1,*], Yan-wei Wang [1], Xin Tang [1] and Zhe Xu [2]

[1] State Key Laboratory of Automotive Simulation and Control, Jilin University, Changchun 130022, China; chuliang@jlu.edu.cn (L.C.); jiayf16@mails.jlu.edu.cn (Y.-f.J.); chends2313@mails.jlu.edu.cn (D.-s.C.); ywwang15@mails.jlu.edu.cn (Y.-w.W.); tangxin16@mails.jlu.edu.cn (X.T.)

[2] R&D Center, China FAW Group Corporation, Changchun 130011, China; xuzhe1@rdc.faw.com.cn

* Correspondence: nanxu@jlu.edu.cn; Tel.: +86-431-8509-5165

Abstract: An open-end winding permanent magnet synchronous motor (PMSM) has a larger range of speed regulation than normal PMSM with the same DC voltage, and the control method is more flexible. It can also manage energy distribution between two power sources without a DC/DC converter. This paper aims at an electric vehicle equipped with OW-PMSM drive system with dual power sources and dual inverters; based on analyzing the external characteristics of each winding mode, we propose a winding mode switching strategy whose torque saturation judgmental algorithm, which is insensitive to motor's parameters, could automatically realize upswitching of the winding mode. The proposed multi-level current hysteresis modulation algorithm could set the major power source and switch it at any time in independent mode, which accomplishes energy distribution between two power sources; its two control methods, low switching frequency method and high power difference method, could achieve different energy distribution effects. Simulation results confirm the validity and effectiveness of the winding mode switching strategy and current modulation method. They also show that an electric vehicle under the proposed control methods has better efficiency than one equipped with a traditional OW-PMSM drive system under traditional control.

Keywords: energy management; electric vehicle; open-end winding permanent magnet synchronous motor (OW-PMSM); multi-level current hysteresis modulation; winding mode switch

1. Introduction

With more rigorous demands for energy savings and environmental protection in industry and the vigorous development of electric vehicles driven by electric motors nowadays, PMSM has become the typical electric motor in electric vehicles because of its advantages such as high-power density and a simple control scheme. In recent years, a drive system constituting an OW-PMSM (open-end winding permanent magnet synchronous motor) and dual inverters has received extensive application [1–5]. This system is actuated via attaching both ends of OW-PMSM's stator windings with an inverter. Compared to the traditional Y-connection PMSM drive system, it has an expanded speed range and a more flexible control method [6–13]; the speed range is larger with the same DC bus voltage, or the DC bus voltage reduces by half with the same speed range. Moreover, it allows dual inverters to use electricity from different electric sources and, when working in a dual electric sources condition, it could manage energy distribution between the two sources without a DC/DC converter [14–16].

Control strategies of OW-PMSM and dual inverters have always been a research focus. Winding topology and configurations are widely discussed in order to optimize the motor's working range and efficiency [17–19]. Fault-tolerant operation [20–22] and zero-sequence voltage elimination method [23,24] are also under extensive research. Loncarski, J. et al. compared the output current ripple in single and dual inverter motor drives for electric vehicles, concluding that the dual-2L inverter can act as a 3L inverter and offers a significant ripple reduction [2], which can also be observed in this paper. AnQun-tao, Sun Li et al. proposed a dual inverters SVPWM modulation method for current control and in this way voltage vector synthesized in the range of a hexagon and when the bus voltage remains constant, the base speed of the electric motor could be 1.7 times that in Y-connection without generating zero-sequence voltage [7,8]. Zhan H., Heng N. et al. studied a common DC bus-based dual inverters SVPWM modulation strategy. In this way, the amplitude of the voltage vector could be maximized and at the same time a zero-sequence current could be suppressed [23,24]. Welchko studied dual sources-based dual inverters' voltage vectors distribution, and proposed three types of voltage distribution methods to adapt to different working conditions of hybrid vehicles to achieve energy management functions between two power sources [16]. However, the two inverters work independently without coordination, and thus the switching frequency of inverter devices has also doubled, which increases the inverter switching loss. All the studies discussed above have proposed current control methods of dual inverters but division of OW-PMSM winding modes and winding modes switching are not involved. Nguyen N.K. et al. studied dual inverters-five-phase OW-PMSM's winding modes, divided into three types, star mode, pentagon mode, and pentacle mode, and analyzed the external motor characteristics of each mode [18]. However, the winding modes are only decided based on rotational speed. A detailed winding modes switching method has not been proposed, nor has there been an analysis of the energy distribution issue between dual sources. Therefore, it is necessary to propose a control method that could manage energy distributions between power sources, and make full use of each winding mode's working range to reduce inverter loss and increase system efficiency for electric vehicles.

This paper first analyzes the three-phase OW-PMSM winding modes division method and the external motor characteristics of each winding mode. On that basis, we propose a torque saturation winding modes switching strategy, which is insensitive to motor parameters, to accomplish automatic winding modes switching according to different working conditions. Then, a multi-level current hysteresis modulation algorithm used in independent mode is put forward. This algorithm could set the major power source and achieve real-time major power source switching to distribute energy between two power sources. In addition, we design two control methods: a low switching frequency method and a high power difference method for different energy distribution purposes. At the end of this paper, the feasibility and effectiveness of the proposed winding modes switching strategy and multi-level current hysteresis modulation are verified through simulations. Vehicle economy performance simulation also showed that the electric vehicle under the proposed control method has better efficiency.

In particular, coordination transformations between the three-phase stator and two-phase rotator in this paper were equivalent power conversions.

2. Winding Mode Features Analysis and Switching Strategy

The dual sources OW-PMSM drive system structure is shown in Figure 1.

According to different winding connections, three-phase OW-PMSM can be divided into three types: star mode, triangle mode, and independent mode. Star mode's winding connection copies traditional PMSMs. It requires heads or tails of three-phase stator windings connected at one point. If it is a dual inverters configuration, it could be completed by making each bridge's lower arm turned on simultaneously in the idle inverter. Triangle mode is accomplished through connecting the heads and tails of three-phase stator windings in a circle. In dual inverters configuration, it could be achieved by shutting down one power source and turning on a triangle circuit switch. Independent mode,

controlled by both sides' inverter bridges of each winding, is a specific one that only OW-PMSM has. It is independent because every winding directly connects with two sides' inverter bridges and there is no direct connection between windings. Independent mode requires both sides' power sources to supply voltage and can accomplish energy flow between power sources through windings.
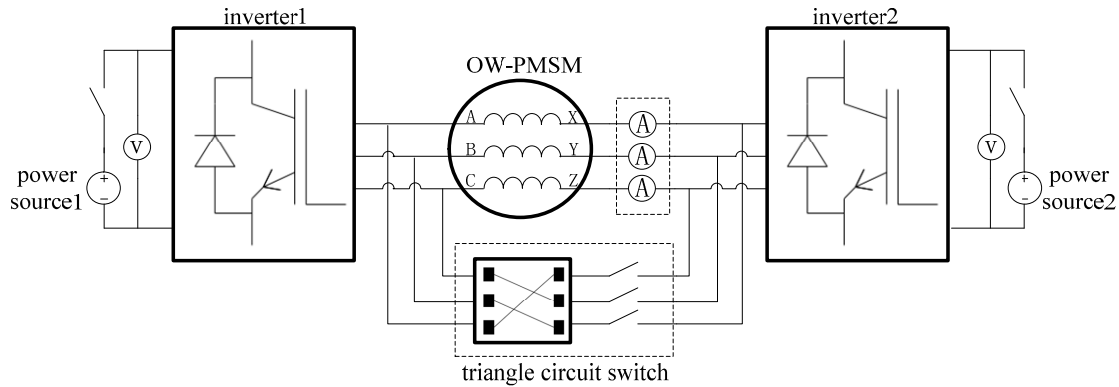

Figure 1. Structure of OW-PMSM drive system.

2.1. Winding Mode Features Analysis

First, we will discuss power source limitations on winding modes. In different winding modes, the maximum amplitude of each winding's phase voltage is different and the connection between each phase is different too, which leads to a difference in basic voltage vectors' amplitude. When the winding mode is star or independent, a certain phase voltage cannot be determined according to the corresponding inverter bridge's switching status and will be influenced by inverter bridges' switching status of other phases due to the load neutral point in star mode and the mid-point potential difference in independent mode floating. For instance, in star mode, when inverter switch statuses are (110) (phase A and B upper bridge arm on, phase C lower bridge arm on), phase voltage relations: $u_A = u_B = V_{dc}/3$, $u_C = -2V_{dc}/3$; when switch statuses are (100), phase voltage relations: $u_A = 2V_{dc}/3$, $u_B = u_C = -V_{dc}/3$. It can be seen that, although phase A's corresponding inverter bridge's switch statuses are the same in both situations, owing to the load neutral point's fluctuation in star mode, phase voltages u_A in both situations are different. Using the schematic diagram of mid-point voltage in Figure 2, we can analyze voltage vectors. We first equally divide power source 1 and power source 2 into two parts according to voltage to determine virtual mid-points m and n. The voltage difference between each inverter bridge's output and the corresponding mid-point is the mid-point voltage and is unaffected by floating neutral potential or mid-point voltage difference. Each inverter bridge's switching status and mid-point voltage has a one-to-one correspondence. The results are identical when using mid-point voltage and phase voltage for voltage vector synthesis.

Star and triangle modes are powered via a single power source and the motor's three-phase stator windings are connected in a specific topology structure. Switching statuses of three-phase inverter bridges can form a voltage vector in the motor space plane. Given that DC bus voltage is V_{dc}, when switching statuses are (110), synthesizing voltage vector in star and triangle modes are shown in Figure 3a,b. Independent mode is powered by dual sources. Supposed that the voltage of power source 1 is V_{dc1} and the voltage of power source 2 is V_{dc2}, when left switch statuses are (110) and right switch statuses are (001), voltage vector synthesis in independent mode is shown in Figure 3c.
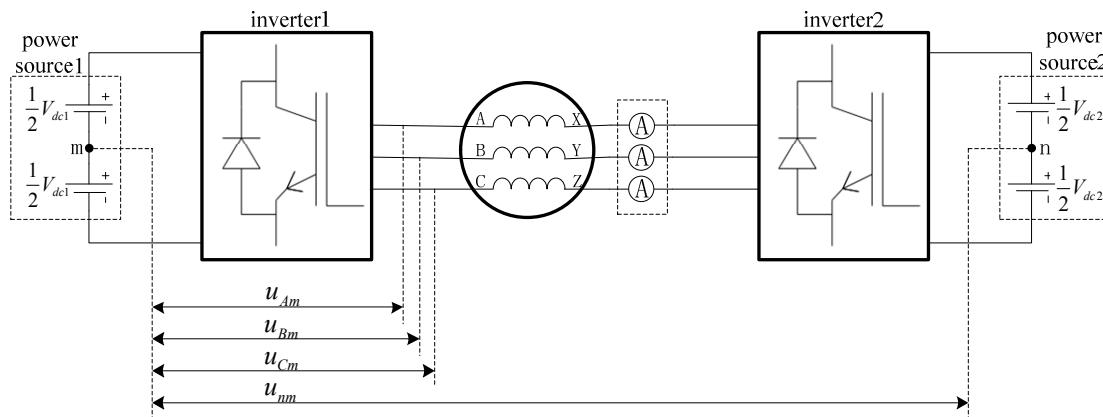
Figure 2. Schematic diagram of mid-point voltage.

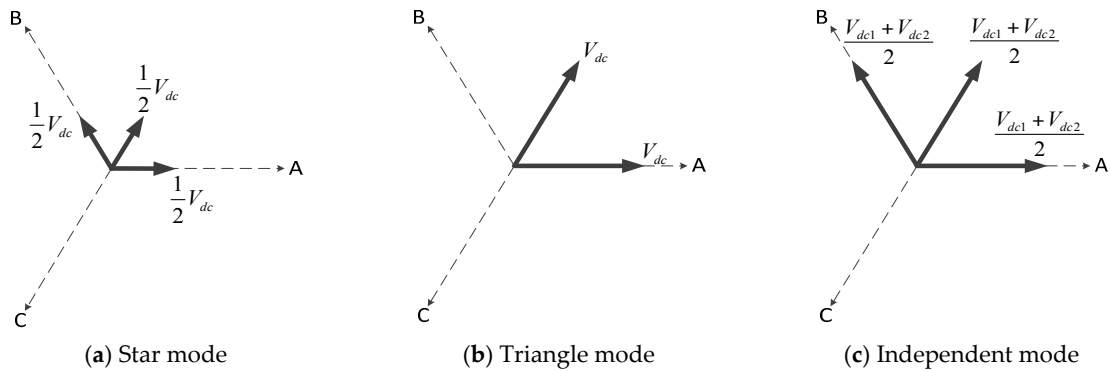| (**a**) Star mode | (**b**) Triangle mode | (**c**) Independent mode |

Figure 3. Synthesizing voltage vector of each winding mode.

The amplitudes of basic voltage vector in star, triangle, and independent modes u_{sbY}, $u_{sb\Delta}$ and u_{sbD} can be obtained from Figure 3 as $\sqrt{2/3}V_{dc}$, $\sqrt{2/3} \times \sqrt{3}V_{dc}$, and $\sqrt{2/3}(V_{dc1} + V_{dc2})$, respectively. In these equations, $\sqrt{2/3}$ is the equal-power conversion coefficient. We can see that when the bus voltage is V_{dc}, the amplitude of the basic voltage vector in triangle mode is $\sqrt{3}$ times that in star mode. In independent mode, when bus voltage $V_{dc1} = V_{dc2} = V_{dc}$, the amplitude of its basic voltage vector is twice that in star mode and $2/\sqrt{3}$ times that in triangle mode. It has to be noted that the above basic voltage vectors are distributed with an $\pi/3$ angle interval, and in each winding mode there are six equal-amplitude basic voltage vectors forming a voltage vector hexagon in the motor vector plane. It is likely that voltage vector may not equal the amplitude of a hexagon vertex's voltage vector in any angle. Hence, the amplitude of the voltage vector in the motor's appropriate linear range is supposed to be the radius of the inscribed circle of a hexagon $\sqrt{3}/2$ times the amplitude of basic voltage vectors when the switch status are as above. Then, the maximum amplitude of the voltage vector at any angle in star, triangle, and independent modes u_{smaxY}, $u_{smax\Delta}$, and u_{smaxD} are: $V_{dc}/\sqrt{2}$, $\sqrt{6}V_{dc}/2$, and $(V_{dc1} + V_{dc2})/\sqrt{2}$, respectively.

Now we will discuss the stator current's limitations on winding modes. Because of windings' inductance characteristics, the phase current of the motor has inertia and cannot abruptly change like voltage. Therefore, in steady state, the waveforms of the three-phase current in the time domain are equal-amplitude sinusoid with $2\pi/3$ phase difference. Three-phase current vectors are demonstrated in Equation (1):

$$\begin{cases} i_A = i\cos(\omega_s t + \phi_1)e^{j0} \\ i_B = i\cos(\omega_s t + \phi_1 - \frac{2\pi}{3})e^{j\frac{2\pi}{3}} \\ i_C = i\cos(\omega_s t + \phi_1 - \frac{4\pi}{3})e^{j\frac{4\pi}{3}} \end{cases} . \tag{1}$$

The synthesized current vector is shown in Equation (2):

$$i_s = \sqrt{\frac{2}{3}}(i_A + i_B + i_C) = \sqrt{\frac{2}{3}} \times \frac{3}{2} i e^{j(\omega_s t + \phi_1)}. \tag{2}$$

It can be observed that the amplitude of the synthesized stator current vector is $\sqrt{3/2}$ times that of the phase current. If we take axis A as a referential axis, the space angle of the current vector corresponds with the phase A current in the time domain. In star and independent modes, the line current of the inverter is the phase current and the current capacity i_{max} is the maximum of the phase current. In triangle mode, line currents i_1, i_2, and i_3 and phase currents i_A, i_B, and i_C have the relationship:

$$i_1 = i_A - i_C, i_2 = i_B - i_A, i_3 = i_C - i_B. \tag{3}$$

According to this relationship, when motors are in steady state, the vector diagrams of line and phase currents in the time domain are as shown in Figure 4.
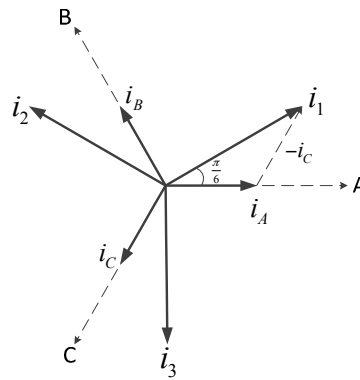

Figure 4. Time domain vector of line current and phase current.

This indicates that, in triangle mode, the amplitude of the line current is $\sqrt{3}$ times that of the phase current in steady state. Consequently, when the current capacity of the inverter is i_{max}, the maximum of the phase current in triangle mode and the maximum amplitude of the synthesized stator current vector is $1/\sqrt{3}$ times that in star and independent modes. In star, independent, and triangle modes, the relationships between maximum amplitude of current vector i_{smaxY}, i_{smaxD}, and $i_{smax\Delta}$ are as shown in Equations (4) and (5):

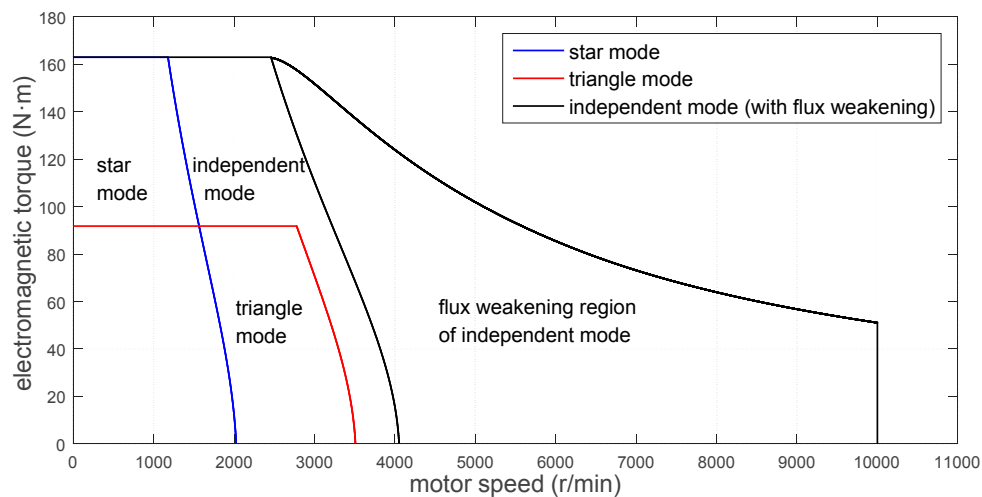$$i_{smaxY} = i_{smaxD} = \frac{\sqrt{6}}{2} i_{max} \tag{4}$$

$$i_{smax\Delta} = \frac{\sqrt{6}}{2} \times \frac{i_{max}}{\sqrt{3}} = \frac{\sqrt{2}}{2} i_{max}. \tag{5}$$

Limitations on voltage and current vectors determine the working ranges of each winding mode. In star and triangle modes, flux-weakening regions are not set. In independent mode, there are non-flux-weakening and flux-weakening regions. In non-flux-weakening regions, if the stator voltage increases to the saturation threshold, the motor starts working in the flux-weakening region to expand the speed regulation range. In the non-flux-weakening region of each winding mode, the motor is controlled by the MTPA (maximum torque per ampere) method [25]. In flux-weakening regions, the motor is controlled by the direct flux control method. Based on the present motor's angular velocity ω_s, the algorithm calculates the specific stator's maximum flux, ψ_s^*. Then, on the basis of requested torque T_e^*, axis d and q's expected current i_d^*, i_q^* are worked out [26].

The OW-PMSM drive system's parameters are shown in Table 1; the external characteristic curves controlled by the above current strategy are demonstrated in Figure 5.

Table 1. Parameters of OW-PMSM drive system.

Items	Parameters
Motor type	Interior open-end winding PMSM
Number of pole pairs p_0	4
Stator resistance R_s/Ω	0.3
Equivalent iron loss resistance R_c/Ω	90
Fundamental amplitude and third harmonic amplitude of permanent magnet flux linkage $[\psi_f, \psi_{f3}]$/Wb	[0.2, 0.01]
d-axis inductance L_d/F	0.0012
q-axis inductance L_q/F	0.0015
Zero sequence inductance L_0/F	0.0003
Rotational inertia of rotor J_m/kgm^{-2}	0.011
Cullen resistance coefficient and viscous resistance coefficient	[0.001, 0.0005]
DC bus voltage of power source 1 V_{dc1}/V	240
DC bus voltage of power source 2 V_{dc2}/V	230
Current capacity of inverter device $i_{\max}$/A	160

Figure 5. External characteristic curves of each winding mode.

We can tell from Figure 5 that the speed regulation range of triangle mode is about $\sqrt{3}$ times that in star mode but the maximum torque is $1/\sqrt{3}$ times that in star mode; the speed regulation range in the non- flux-weakening region in independent mode is approximately twice that in star mode and its maximum torque is equal to that in star mode.

2.2. Winding Modes Switching Strategy

We first determine general winding modes switching strategies. When the motor is in star or triangle mode, only one inverter is working with on-state losses and switching losses. When another inverter has lower bridge arms on, there is only on-state loss. In triangle mode, it is different than when the triangle circuit switch is turned on; there are on-state losses on triangle circuit. What is more, the topology of stator winding in triangle mode determines probable zero-sequence current in the motor, which may contribute to wastage of the inverter's current capacity and losses on electric resistance and electronic devices due to the current's heating effect. In independent mode, both sides' inverters are working and have on-state losses and switching losses. In conclusion, in terms of losses in electronic devices, star mode has the least and independent mode has the most, with triangle mode in the middle. In order to reduce those losses in electronic devices, the general winding modes switching strategy might be that if working conditions are appropriate, star mode is the first choice, then triangle mode; try not to use independent mode.

Under most circumstances, the differences between both sides' DC bus voltage are small and the highest rotary speeds of the motor in the non-flux-weakening region, triangle and independent mode increase in the order $n_{mY} < n_{m\Delta} < n_{mD}$. In accordance with this inequality, we define switching from star mode to triangle mode, from triangle mode to independent mode, and from star mode to independent mode as upswitching; switching from independent mode to triangle mode, from triangle mode to star mode, and from independent mode to star mode are downswitching.

We will begin with the upswitching strategy. During motor working period, parameters such as magnet flux and inductance fluctuate because of rising temperature, followed by fluctuations of working ranges of each winding mode. To avoid frequent switching when the working point of the motor fluctuates, this paper proposes an algorithm to judge the saturation state of torque. When judged as positive, upswitching is triggered to ensure the accuracy of the switching boundary.

This algorithm functions during the process of torque increasing from zero to the maximum. It calculates when the expected torque is at a maximum, the time period t_{int} during which torque increases from zero to the maximum at this specific rotary speed in the current winding mode (star or triangle) as integration time and integration of absolute torque error ΔT (the difference between actual torque T_l and expected torque T_e^*) as threshold I_{th} in this process. Then, it calculates integration I of absolute actual torque error ΔT from t_{int} to the present and compares it with integration threshold I_{th}. If $I \geq I_{th}$, then the motor's torque is almost saturated and does not match the expected torque. This algorithm is based on whether the output torque agrees with the expected torque in a particular period to eliminate uncertainties in the winding modes' working range because of fluctuations in the motor's parameters.

Voltage equations of motor in dq coordination are expressed in Equations (6) and (7):

$$u_d = R_s i_d + L_d \frac{di_d}{dt} - \omega_r L_q i_q \tag{6}$$

$$u_q = R_s i_q + L_q \frac{di_q}{dt} + \omega_r (L_d i_d + \psi_f). \tag{7}$$

Electromagnetic torque is shown in Equation (8):

$$T_e = p_0 i_q [\psi_f + (L_d - L_q) i_d]. \tag{8}$$

From the above equations, we can tell that electromagnetic torque T_e is mainly determined by axis q's current i_q; the smaller the inductance difference between axis d and q, the bigger the share that i_q determines. When $L_d = L_q = L_s$ the motor is surface-mounted; MTPA control is $i_d = 0$ control. For the sake of simplifying calculations, the integration time of torque t_{int} is derived as $i_d = 0$ control, and when the difference between L_d and L_q is small, MTPA control is still accurate using t_{int}. In addition, because $L_q \geq L_d$, the inertia of i_q is higher and the change rate of i_q is smaller if applied with the same voltage, which makes the calculated integration time t_{int} is bigger and the threshold of torque saturation is higher.

When using $i_d = 0$ control, due to the current of axis d being 0, voltage equations and torque expression of motor in dq coordination have changed to:

$$u_d = -\omega_r L_q i_q \tag{9}$$

$$u_q = R_s i_q + L_q \frac{di_q}{dt} + \omega_r \psi_f \tag{10}$$

$$T_e = p_0 \psi_f i_q. \tag{11}$$

Voltage vectors have the relationship:

$$u_s^2 = u_d^2 + u_q^2 = (-\omega_r L_q i_q)^2 + \left(R_s i_q + L_q \frac{di_q}{dt} + \omega_r \psi_f \right)^2. \tag{12}$$

When the voltage vector is at its maximum u_{smax}, we can get the change rate of axis q's current from Equation (13):

$$\frac{di_q}{dt} = \frac{\sqrt{u_{smax}^2 - (\omega_r L_q i_q)^2} - \omega_r \psi_f - R_s i_q}{L_q}. \tag{13}$$

In Equation (13), because of the mechanical inertia being greater than the electronic inertia, we can assume that ω_r is constant during torque integration time t_{int}, but during this time i_q increases from 0 to the maximum of stator current vector amplitude, i_{smax}. In order to simplify the torque following process into a linear process, di_q/dt must be a constant. By maximizing i_q to i_{smax}, we can get the minimum of di_q/dt for an increased integration time and thus a higher torque saturation threshold. If we neglect stator electric resistance R_s, then we get di_q/dt as:

$$\frac{di_q}{dt} = \frac{\sqrt{u_{smax}^2 - (\omega_r L_q i_{smax})^2} - \omega_r \psi_f}{L_q}. \tag{14}$$

It is obvious that with motor rotary velocity ω_r increasing, the partial voltage of electromotive force increases, voltage of stator gets almost saturated, and the voltage allowance used to control motor cuttent decreases, which in turn results in diminishing di_q/dt. When ω_r approaches the right boundary of the non-flux-weakening region's external characteristics in current winding mode, di_q/dt slips to 0, implying that the drive system is losing control of the motor's current. In order to guarantee a certain amount of voltage margin used to control the motor's current, we, in accordance with base speed ratio, can get the motor angular velocity ω_{rs} used to calculate di_q/dt in each winding mode by Equation (15):

$$\omega_{rs} = k_s \omega_{rb}. \tag{15}$$

In Equation (15), ω_{rb} is the rotator's base angular velocity of the motor in current winding mode. When ignoring R_s in $i_d = 0$ control strategy, we can get:

$$\omega_{rb} = \frac{u_{smax}}{\psi_s} = \frac{u_{smax}}{\sqrt{\psi_f^2 + (L_q i_{smax})^2}}. \tag{16}$$

Because the approximation of di_q/dt is constant, the integration time t_{int} of this process is:

$$t_{int} = \frac{\Delta i_q}{di_q/dt} = \frac{L_q i_{smax}}{\sqrt{u_{smax}^2 - (\omega_{rs} L_q i_{smax})^2} - \omega_{rs} \psi_f} = \frac{L_q i_{smax}}{\sqrt{u_{smax}^2 - (k_s \omega_{rb} L_q i_{smax})^2} - k_s \omega_{rb} \psi_f}. \tag{17}$$

In Equation (17), k_s is the rotator speed sensitivity coefficient and $k_s \in (0,1)$; the bigger k_s is, the closer the motor's angular velocity $k_s \omega_{rb}$ used to calculate integration time t_{int} is to the current winding mode's base angular velocity, and the smaller voltage margin and di_q/dt are, which leads to bigger t_{int} and vice versa. k_s reflects tolerance of torque following speed. The bigger k_s is, the lower the requirements for torque following speed, which leads to a slower response of the torque saturation judgmental algorithm. In the above two expressions, i_{smax} is the maximum of the stator current vector in the present winding mode and u_{smax} is the maximum of any angle voltage vector in the present winding mode.

Because the approximation of di_q/dt is constant, the torque following process is simplified to a linear process. The integration of torque error of this process is:

$$I_{lim} = \int_0^{t_{int}} |\Delta T dt| = \int_0^{t_{int}} |T_l - T_e^*| dt = \frac{1}{2} T_{emax} t_{int}. \tag{18}$$

For practical application, we define an integration threshold sensitivity coefficient so that the actual integration threshold is:

$$I_{th} = k_I I_{\lim} = \frac{1}{2} k_I T_{e\max} t_{int} = \frac{1}{2} k_I p_0 \psi_f i_{s\max} t_{int}. \tag{19}$$

In Equation (19), $T_{e\max}$ is the maximum electromagnetic torque in the current winding mode. For integration threshold sensitivity coefficient $k_I \in (0,1)$, the bigger k_I is, the bigger integration threshold I_{th} is and the less sensitive the judgment of torque saturation, which can reduce the possibility of improper switching but will also increase delays in winding mode switching; the smaller k_I is, the smaller integration threshold I_{th} is and the more sensitive the judgment of torque saturation, which can make torque switching swift but may lead to improper switching when working conditions change unexpectedly. By changing k_s and k_I, we can modulate the sensitivity and stability of the torque saturation judgmental algorithm.

It is important to note that if the current mode is triangle mode, upswitching's goal is only independent mode; when the torque saturation threshold is reached, the current mode is switched to independent mode. However, if the current mode is star mode, there are two options: triangle and independent mode; when the torque saturation threshold is reached, terminals are decided by the degree of saturation of stator current vector. When the amplitude of stator current vector $i_s \geq i_{s\max\Delta}$, it indicates that the amplitude of the stator current vector in the current mode exceeds the capacity of adjustment of triangle mode and upswitching's goal is independent mode; when $i_s < i_{s\max\Delta}$, the goal is triangle mode.

Downswitching is determined by the rotary speed threshold, which is the base speed of each winding mode. When the motor's rotary speed decreases to the star or triangle mode's base speed, downswitching is triggered. This strategy staggers the working points of upswitching and downswitching to avoid frequent switching. Switching is not only decided by the motor's speed, like upswitching, but also by the degree of saturation of the stator current vector. Whether the current mode is triangle or independent, as long as the motor's speed has the relationship $n_r < n_{bY}$ the motor's speed is lower than the star mode's base speed, and the current mode is switched to star mode. However, if the current mode is independent and the motor's speed has the relationship $n_{bY} < n_r < n_{b\Delta}$, it has to be decided whether to switch to triangle mode or not. When the amplitude of stator current vector $i_s \geq i_{s\max\Delta}$, this indicates that the amplitude of the stator current vector has exceeded the capacity of adjustment of triangle mode and current winding should stay in independent mode. If $i_s < i_{s\max\Delta}$, the current mode is switched to triangle mode.

Switching principles among the three winding modes are summarized in Table 2.

Table 2. Switching algorithm of each winding mode.

Switching Goal / Starting Mode	Star Mode	Triangle Mode	Independent Mode
Star mode	NA	Positive torque saturation decision and $i_s < i_{s\max\Delta}$	Positive torque saturation decision and $i_s \geq i_{s\max\Delta}$
Triangle mode	$n_r < n_{bY}$	NA	Positive torque saturation decision
Independent mode	$n_r < n_{bY}$	$n_{bY} \leq n_r < n_{b\Delta}$ and $i_s < i_{s\max\Delta}$	NA

3. Dual Inverters' Current Modulation Method

This paper adopts a hysteresis control-based current control method. In single-sourced star and triangle modes, inverters could only provide two potentials for each winding. Thus, the traditional hysteresis current control method was adopted. In dual-sourced independent mode, dual inverters, when controlled coordinately, could provide three or four potentials. Hence, a multi-level hysteresis current control method was employed.

3.1. Current Modulation Method in Star and Triangle Modes

Star mode required ends of three-phase stator windings connected to one point, which could be accomplished by making all lower arms of the idle inverter's bridges turned on at the same time in dual inverters configuration while the other inverter was working to control the three-phase current. Based on expected torque T_e^*, we could get control variables i_d^* and i_q^* through the abovementioned MTPA and flux-weakening strategy. Then, with dq0 to ABC coordination transformation, expected phase currents i_A^*, i_B^* and i_C^* were obtained; meanwhile, actual phase currents i_A, i_B, and i_C were acquired via the current sensor. Phase current error represented the difference between each phase expected current and the actual current, which is demonstrated by following formula:

$$\Delta i_A = i_A - i_A^*, \Delta i_B = i_B - i_B^*, \Delta i_C = i_C - i_C^*. \tag{20}$$

From each phase current's error, we could control the three-phase current. Given the half-width of the current's hysteresis band, the acceptable current error is h. When one phase current error $\Delta i \geq h$, the upper arm of this phase's inverter bridge was turned off and the lower arm was turned on, making the midpoint voltage of this phase $-V_{dc}/2$, a lower voltage, and the phase current error Δi of this phase decreasing. When phase current error $\Delta i \leq -h$, the upper arm of this phase's inverter bridge was turned on and the lower arm was turned off, making the midpoint voltage of this phase $V_{dc}/2$, a lower voltage, and the phase current error Δi of this phase increasing.

Triangle mode requires the heads and tails of three-phase stator windings to be connected in a circle, which is completed by shutting down one power source and turning on triangle circuit switch. The other side's inverter was working to control the motor's current. What was different from star mode was that triangle mode, instead of controlling the motor's phase current i_A, i_B, and i_C directly, controlled motor's line current i_1, i_2, and i_3 to control motor's phase current indirectly. The relationship of triangle mode's phase current and line current is shown in Equation (3). With Equation (3), we can transform phase current's expected value i_A^*, i_B^*, and i_C^* to line current's expected value i_1^*, i_2^*, and i_3^*, then determine line current's error Δi_1, Δi_2, and Δi_3 to have each line current hysteresis controlled respectively.

If ignoring zero-sequence current in triangle circuit, we got $i_A + i_B + i_C = 0$, and then we could get the phase current expression, represented by the line current as Equation (21) via Equation (3):

$$i_A = (i_1 - i_2)/3, i_B = (i_2 - i_3)/3, i_C = (i_3 - i_1)/3. \tag{21}$$

If the acceptable line current error was h_l, the half-width of the hysteresis band of i_1, i_2 was h_l, and the acceptable error of $i_1 - i_2$ was $2h_l$, then we could calculate the acceptable error of phase current $i_A = (i_1 - i_2)/3$ as $2h_l/3$. Thus, it was clear that if the acceptable error of phase current stayed at h, the line current hysteresis comparator's acceptable current error was required to be set at $3h/2$, so we had:

$$h_l = 3h/2. \tag{22}$$

At this point, if ignoring the zero-sequence current, the tracking error of the phase current in triangle mode was the same as that in star mode. However, note that the topology of triangle mode is different from that of star mode and DC bus voltage was directly loaded on the phase current. In every combination of inverter switching states, there are five possible phase voltages in star mode: $-2V_{dc}/3$, $-V_{dc}/3$, 0, $V_{dc}/3$, $2V_{dc}/3$. In triangle mode, there are three possible phase voltages with higher amplitude: $-V_{dc}$, 0, V_{dc}. Therefore, if the half-width of the hysteresis band was determined according to Equation (22), even though the acceptable tracking error of the current in triangle mode was the same as that in star mode, the current saw tooth fluctuation in triangle mode is more drastic than that in star mode and the switching frequency of inverters, along with the core loss of motor, would be greater than those in star mode.

3.2. Current Modulation Method in Independent Mode

Different from star and triangle modes, independent mode is powered by two sources and controlled by two inverters, which means each winding's electric potential is controlled by both of the two inverters' bridges and has four statuses: (10), (01), (11), and (00).

The first number of switching status stands for the electric potential of inverter 1's bridge. The second number of switching status stands for the electric potential of inverter 2's bridge. The status of the inverter bridge upper arm (on) and lower arm (off) obtained high potential, which was substituted with number "1". The status of the inverter bridge upper arm (off) and lower arm (on) obtained low potential, which was substituted with number "0". Because the two sources were insulated, the mid-point voltage difference of the two sources u_{nm} varied with different inverter switching statuses, which brought about diverse phase voltages in different switching statuses, especially when $V_{dc1} \neq V_{dc2}$. When the mid-point voltage of the two sources was $u_{nm} = 0$, the phase voltage was the mid-point phase voltage. When the switching statuses were (10), (01), (11), and (00), the corresponding mid-point phase voltages were $(V_{dc1} + V_{dc2})/2$, $-(V_{dc1} + V_{dc2})/2$, $(V_{dc1} - V_{dc2})/2$, and $-(V_{dc1} - V_{dc2})/2$. Hence, when $V_{dc1} \neq V_{dc2}$, we could get four mid-point voltages via dual inverters' control. When $V_{dc1} = V_{dc2}$, we could get three mid-point voltages and the mid-point voltages with switching statuses (11) and (00) were both zero.

The traditional hysteresis current modulation algorithm has two potentials and corresponding two trigger areas: $\Delta i \geq h$ and $\Delta i \leq -h$. When $V_{dc1} \neq V_{dc2}$, there are four potentials in independent mode of the hysteresis current modulation algorithm. Apart from two trigger areas used for activating switching statuses (01) and (10), two intermediate trigger lines were needed for activating switching statuses (00) and (11)—two intermediate potentials. Provided the two intermediate trigger lines were $\Delta i = d$ and $\Delta i = -d$, with d as the linear current deviation of the intermediate line, we could get Equation (23) based on the principle that mid-point voltage is proportional to current error Δi when triggered:

$$h : \frac{V_{dc1} + V_{dc2}}{2} = d : \frac{V_{dc1} - V_{dc2}}{2}. \tag{23}$$

Equation (23) could be transformed to:

$$d = \frac{V_{dc1} - V_{dc2}}{V_{dc1} + V_{dc2}} h. \tag{24}$$

It was obvious that when $V_{dc1} > V_{dc2}$, $d > 0$; when $V_{dc1} < V_{dc2}$, $d < 0$; when $V_{dc1} = V_{dc2}$, $d = 0$, and at this time, two intermediate trigger lines coincided at $\Delta i = 0$. It has to be pointed out that in each winding's four potentials in independent mode, two boundary potentials are triggered by Δi being in the corresponding area to ensure that Δi can depart from that triggered area swiftly in the relatively greater phase voltage generated by boundary potentials as long as Δi is in the corresponding area and restricted to hysteresis band $[-h, h]$. Two intermediate potentials were triggered by crossing the corresponding intermediate trigger lines without considering the crossing direction; this control logic mainly mattered in slowing fluctuations of Δi down to load smaller voltage. A rather small phase voltage would be loaded if Δi is close to the center line ($\Delta i = 0$) to avoid drastic fluctuations frequently hitting the hysteresis boundary if constantly loaded with large phase voltage. When applied with this modulation method, the changing rate would decrease after Δi crosses the control line $\Delta i = d$ or $\Delta i = -d$ until it hits the boundary again. Two additional potentials would effectively retard the fluctuation speed of Δi to make current changes milder and reduce the inverters' switching frequency.

Two improved multi-level hysteresis modulation methods were proposed on the foundation of the above multi-level hysteresis current modulation strategy. They were the low switching frequency method and high power difference method. These two methods were achieved by adding the trigger conditions of inverter bridges' switching statuses (00) and (11) in independent mode.

Due to independent mode being powered by two sources, power distribution between two sources was involved. Thus, a major power source was proposed and was expected to have greater

power output than the other source in independent mode. Low switching frequency and high power difference methods could determine which one was the major power source and switch over it at any time to accomplish power distribution. When the load is low, the major power source can even charge another source. Table 3 indicates the relationships between inverter bridges' switching statuses, direction of phase current *i*, and current flow. Given that phase current flowing from left to right is positive in Figure 1, we could tell that energy flow between the two sources could only be accomplished when the inverter bridges' switching statuses were at two intermediate potentials (00) and (11).

Table 3. Relationship between inverter bridge's switching states and power flow direction.

Inverter Switching States	Direction of Phase Current	$i < 0$	$i > 0$
Boundary potentials	(01)	Both power sources discharging	Both power sources charging
	(10)	Both power sources charging	Both power sources discharging
Intermediate potentials	(00)	Power source 1 discharging Power source 2 charging	Power source 1 charging Power source 2 discharging
	(11)	Power source 1 charging Power source 2 discharging	Power source 1 discharging Power source 2 charging

The trigger regulation of inverter bridges' switching statuses in low switching frequency and the high power difference method is displayed in Table 4.

Table 4. Dual inverter trigger rules of two different current modulation methods.

Inverter Switching States	Modulation Pattern	Low Switching Frequency Method	High Power Difference Method
Boundary potentials	(01)	Δi is in the area of $\Delta i \geq h$	Δi is in the area of $\Delta i \geq h$
	(10)	Δi is in the area of $\Delta i \geq h$	Δi is in the area of $\Delta i \geq h$
Intermediate potentials	(00)	Δi crossed control line $\Delta i = d$ and switching state of inverter bridge on major power source's side is 0	Δi crossed control line $\Delta i = d$ and when power source 1 is major power source: phrase current $i < 0$; when power source 2 is major power source: phrase current $i > 0$
	(11)	Δi crossed control line $\Delta i = -d$ and switching state of inverter bridge on major power source's side is 1	Δi crossed control line $\Delta i = -d$ and when power source 1 is major power source: phrase current $i > 0$; when power source 2 is major power source: phrase current $i < 0$

These two improved methods added trigger conditions of two intermediate potentials, which made two potentials, instead of being triggered when Δi crossing control lines $\Delta i = \pm d$, triggered at other specific conditions. Normally only one intermediate potential was triggered in one hysteresis period. The low switching frequency method, needed to confirm the switching status of inverter bridge on major power source's side, remains unchanged after switching when Δi crossing control lines $\Delta i = \pm d$. In this case, the switching statuses of both two inverters' bridges would not be changed simultaneously when Δi crosses the control lines and the switching frequency of inverter devices could be lowered to a minimum. In the high power difference method, when Δi crosses the control lines $\Delta i = \pm d$, we need to decide whether to switch based on the present phase current *i*'s direction to ensure the major power source could charge the other source when the switching status of inverter bridge is at two intermediate potentials. This method increases the difference between two sources' power outputs as much as possible.

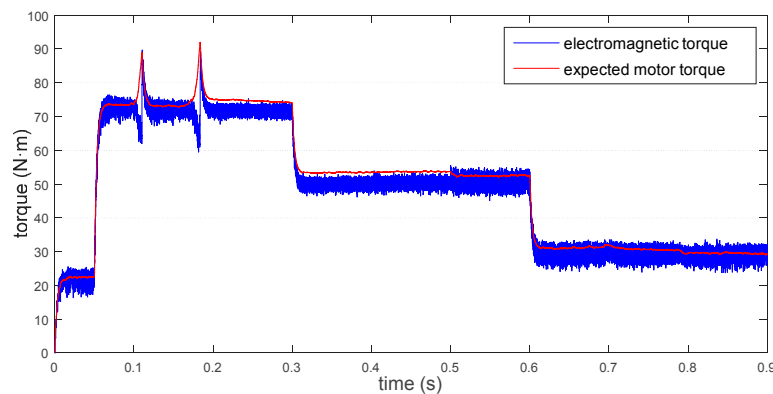## 4. Results of Simulations of OW-PMSM Drive System

We ran simulation models of the OW-PMSM drive system on the Matlab/Simulink platform. The basic parameters of OW-PMSM are shown in Table 1 and controller parameters are shown in Table 5. A PI speed controller was used to generate the expected torque to make the motor speed follow the preset value.

Table 5. Parameters of simulation setting and controller.

Module Affiliation	Item	Parameters
Model as a whole	Time step T_s/s	5×10^{-7}
Inverter devices	On-resistance R_{on}/Ω	0.01
	Forward voltage drop of IGBT V_f/V	0.8
	Forward voltage drop of diode V_{fd}/V	0.8
	Current fall time T_f/s	1×10^{-6}
	Current tailing time T_t/s	1.5×10^{-6}
Winding mode controller	Sampling time T_{s_MS}/s	1×10^{-4}
	Sensitivity coefficient of rotor speed $[k_{sY}, k_{s\Delta}]$	[0.9, 0.9]
	Sensitivity coefficient of integral threshold $[k_{IY}, k_{I\Delta}]$	[0.35, 0.75]
PI controller of motor speed	Sampling time T_{s_SC}/s	1×10^{-4}
	Proportionality coefficient P	0.4
	Integral coefficient I	4
MTPA and flux weakening controller	Sampling time T_{s_CC}/s	1×10^{-4}
	Voltage saturation coefficient k_u	0.95
Current hysteresis controller	Sampling time T_{s_CR}/s	1×10^{-5}
	Half width of hysteresis band h/A	3
	Maximum switching frequency of devices f_{max}/Hz	1×10^4

This simulation's duration was 0.9 s. In this process, the expected motor rotary speed linearly increased to 5500 r/min in 0–0.3 s and stayed at 5500 r/min till 0.6 s. Then speed linearly dropped to 0 in 0.6–0.9 s; loaded torque jumped from 0 to 50 N·m at 0.05 s and remained 50 N·m until the simulation finished. In order to monitor the results of power distribution, we shifted the current modulation method from low switching frequency to high power difference at 0.4 s and switched the major power source from power source 1 to power source 2 at 0.5 s. Another OW-PMSM drive system under traditional two-level current hysteresis modulation without winding mode switching function was also simulated for comparison.

Curves of expected torque T_e^*, electromagnetic torque T_e of proposed and contrast model, and rotary speed n_m are demonstrated in Figure 6a–c.

(**a**) Expected torque and electromagnetic torque of motor

Figure 6. *Cont.*

(**b**) Electromagnetic torque of motor in contrast model
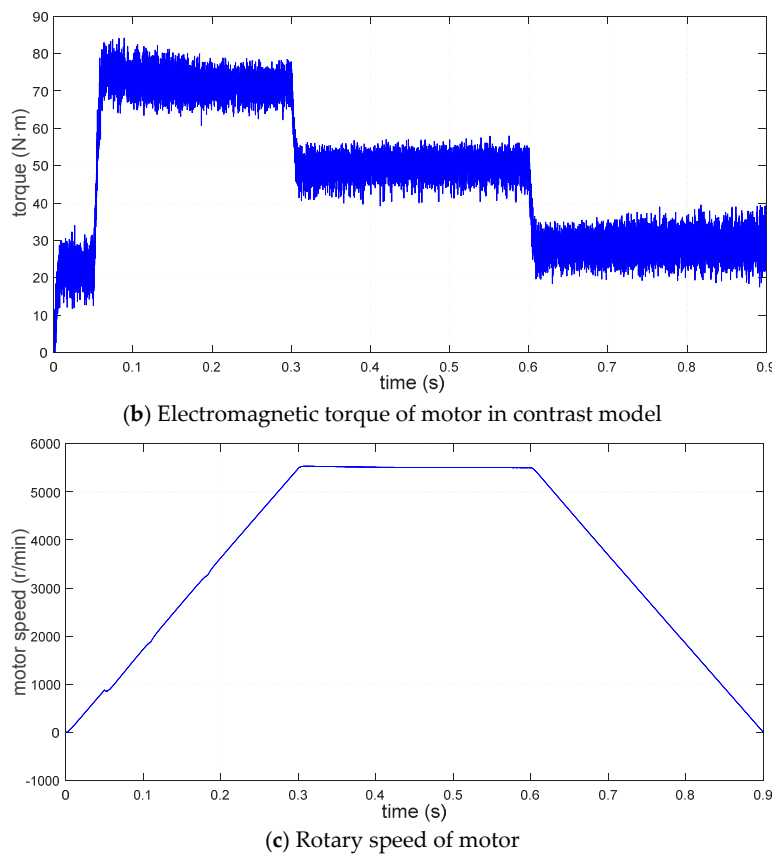

(**c**) Rotary speed of motor

Figure 6. Curves of expected motor torque, electromagnetic torque, and motor speed.

We understand from Figure 6 that the motor rotary speed could smoothly and swiftly follow the preset value and only had a slight fluctuation at 0.05 s when the loaded torque jumped. Switching of modes had no impact on rotary speed. Electromagnetic torque T_e could also follow expected torque T_e^* well. In the present current following accuracy (h = 3 A), the amplitude of electromagnetic torque's fluctuation was limited within 5 N·m or so, but after switching to lower voltage power source 2 as major power source, the fluctuation was more drastic, which indicated that setting the higher voltage power source as the major power source is preferable. We also found that the motor under the proposed multi-level current hysteresis modulation had about 30% less torque fluctuation than the motor under traditional two-level current hysteresis modulation.

Winding mode, torque saturation judgmental threshold I_{th}, and actual integration I curves are displayed in Figure 7a,b.

In Figure 7a, the mode signals are demonstrated: 1 is star mode, 2 stands for triangle mode, 3 and 4 are the low switching frequency and high power difference methods, respectively, in independent mode, and 3.5 and 4.5 represented the flux-weakening region of the two methods, respectively, in independent mode. In Figure 6a,b, two peaks of expected torque curve at 0.12 s and 0.17 s indicate that with increasing speed, voltage is almost saturated and electromagnetic torque cannot follow expected torque, leading to the speed controller further increasing the expected torque; from the electromagnetic torque curve, it is evident that the actual electromagnetic torque will gradually decline because of voltage saturation before the expected torque peak; when torque error accumulates enough to satisfy torque saturation conditions, upswitching is triggered and electromagnetic torque rapidly follows the expected torque after switching; From electromagnetic torque being unable to follow to the upswitching point, it only took 0.02 s. From Figure 7b, we understand that 0.02 s before upswitching, with the voltage almost saturated, the switching integration of torque error rose sharply to the threshold and upswitching was triggered. After winding mode switching to triangle mode from

star mode, the integration threshold and integration of torque error declined due to the integration time being smaller.
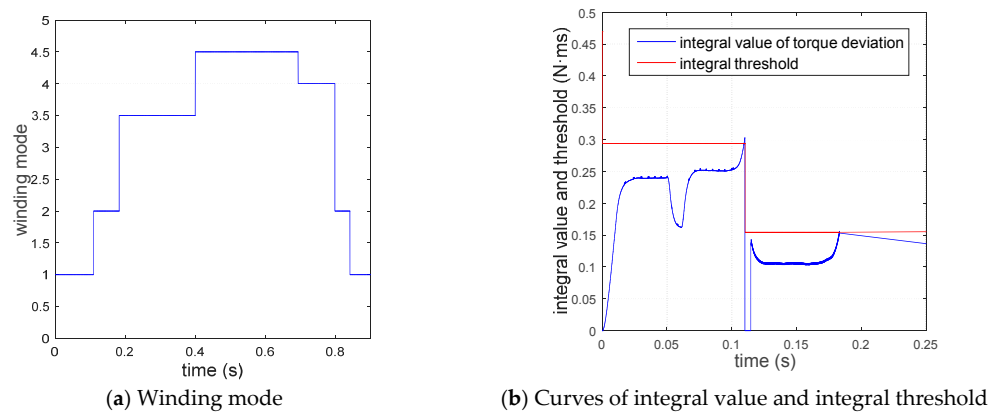

(**a**) Winding mode

(**b**) Curves of integral value and integral threshold

Figure 7. Curves of winding mode, integral value, and threshold of torque saturation decision.

Phase A's voltage curves at star and triangle, and triangle and independent mode switching points are shown in Figure 8a,b. Phase A's current and its local curves are shown in Figure 8c,d.
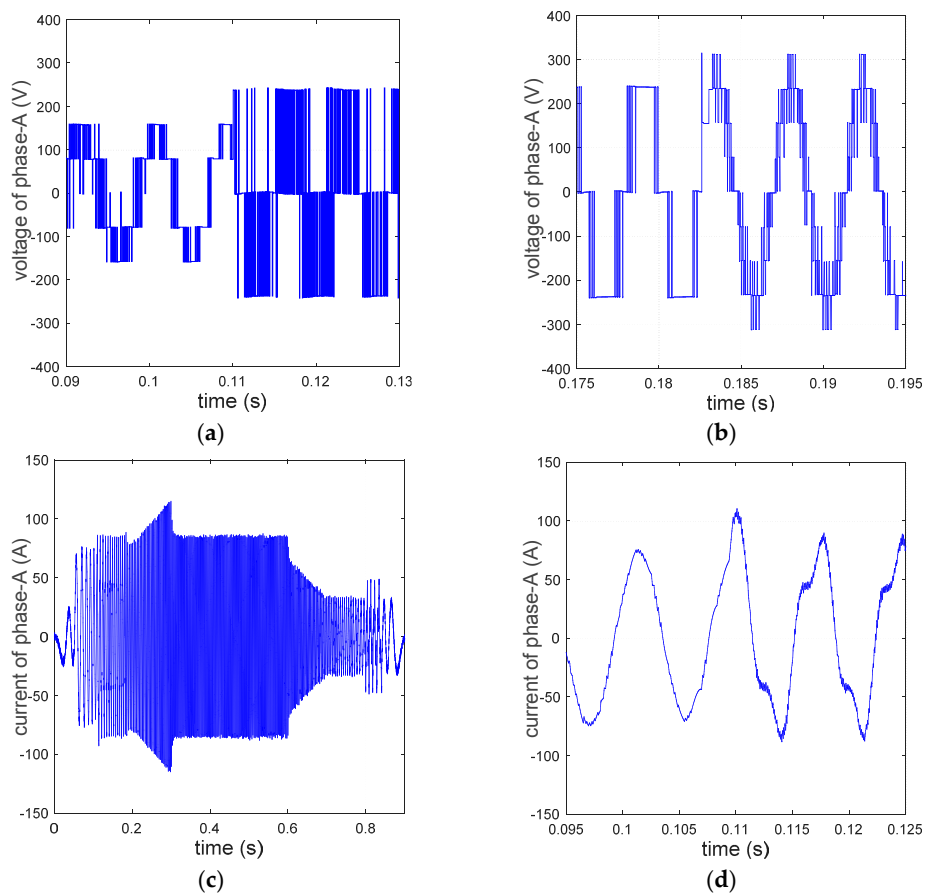

(**a**)

(**b**)

(**c**)

(**d**)

Figure 8. Curves and partial waves of phase A's voltage and current. (**a**) Partial wave of phase—A voltage at switching point 1; (**b**) partial wave of phase—A voltage at switching point 2; (**c**) curve of Phase—A current; (**d**) partial wave of phase—A current at switching point 1.

It is clear that the phase voltage of motor changes follows a sinusoidal waveform; amplitudes of phase voltage in star, triangle and independent modes increased in sequence. From the local curve of phase A's voltage, there were five phase voltage values, $-2V_{dc}/3$, $-V_{dc}/3$, 0, $V_{dc}/3$, and $2V_{dc}/3$, when the motor was in star mode. There were only three phase voltage values, $-V_{dc}$, 0, and V_{dc}, when the motor was in triangle mode; if we ignore the voltage difference between the two sides' power sources, there were nine phase voltage values, $-4V_{dc}/3$, $-V_{dc}$, $-2V_{dc}/3$, $-V_{dc}/3$, 0, $V_{dc}/3$, $2V_{dc}/3$, V_{dc}, and $4V_{dc}/3$ when the motor was in independent mode, which made the current control more smooth. The phase current of the motor changed according to the sinusoidal rule; because of the zero-sequence current effect, the amplitude of the phase current in triangle mode was slightly greater than those in star and independent modes with the same amplitude of stator's current. From Figure 8d, we can see that after switching from star mode to triangle mode, the waveform of phase current changed and was no longer a standard sinusoidal waveform due to the zero-sequence current, which led to occupation of the inverter's extra capacity and increasing switching frequency of devices. At the same time, the phase current was restricted in the hysteresis band and the current followed accordingly.

Total switching frequency of inverter devices (sum of all IGBT devices' switching frequencies) of both the proposed and the contrasting model is shown in Figure 9a. Inverters' loss is shown in Figure 9b.
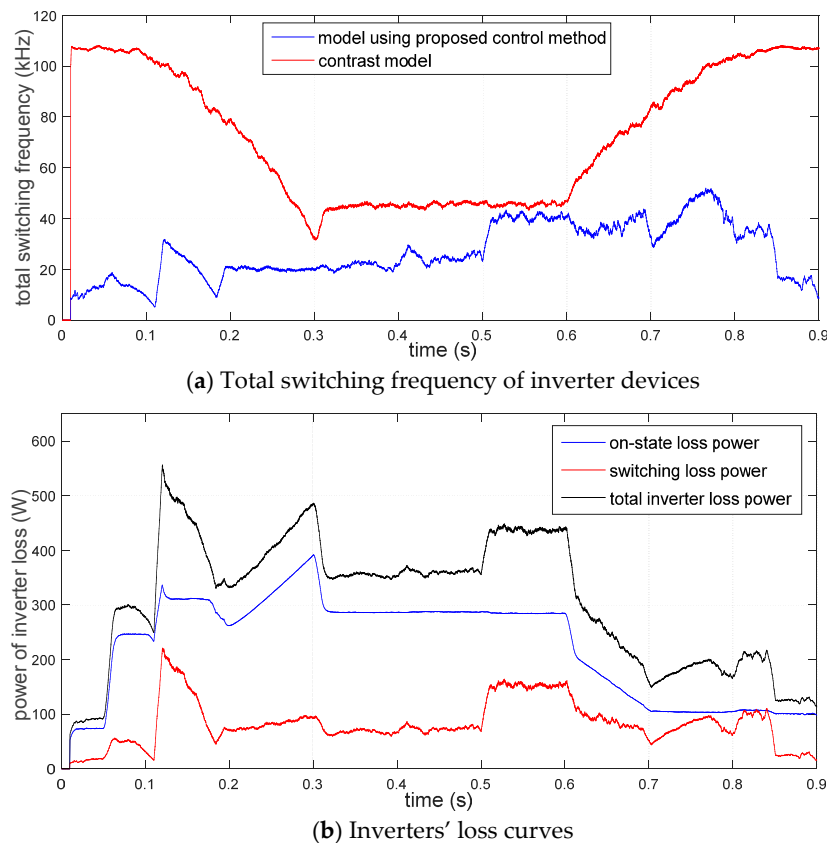

(**a**) Total switching frequency of inverter devices

(**b**) Inverters' loss curves

Figure 9. Curves of total switching frequency of inverter devices and inverter loss.

From Figure 9a, we see that the switching frequencies of inverter devices in triangle mode are higher than those in star mode because the phase voltage values in triangle mode are lower and their amplitudes were greater, leading to a higher changing rate of phase current and more frequently hitting the hysteresis boundary; the total switching frequency of inverter devices in independent mode is also high due to the two inverters working together in independent mode. However, there were more phase voltage values in independent mode and the control of the phase current could be more smooth

and flexible, which might reduce the switching frequencies of inverter devices. The total switching frequency of devices increased after shifting from the low switching frequency method to the high power difference method at 0.4 s; the total switching frequency increased even more after switching the major power source from power source 1 to power source 2, a lower voltage power source, at 0.5 s, which indicated that setting a higher voltage power source as the major power source could reduce the switching frequencies of devices. In addition, the total switching frequency of devices in steady state was lower than that in transient state and it was higher when the motor speed was decreasing than when motor speed was increasing. Under the proposed control method, total switching frequency is far lower than in the contrasting model, especially in the period of star and triangle mode. In Figure 9b, the switching loss of inverters was proportional to the total switching frequency of devices and in most circumstances the share of switching losses of inverters was under 30%, which was ideal.

Input power curves of both inverters are shown in Figure 10.

It was evident that before 0.5 s, power source 1 was the major power source; in this period, star mode and triangle mode were all powered by power source 1 and all input power was generated by inverter 1; after 0.5 s, power source 2 was the major power source. In this period, star mode and triangle mode were supplied by power source 2 and all input power was generated by inverter 2. When in independent mode, both power sources provided power. After shifting from the low switching frequency method to the high power difference method at 0.4 s, the power difference between two inverters increased; after switching the major power source from power source 1 to power source 2 at 0.5 s, inverter 2's power was higher than inverter 1's, becoming the major power output inverter; nevertheless, because of the voltage of power source 2 being lower than that of power source 1, after switching the major power source to power source 2, the power difference between two inverters decreased, which indicated that the power difference of the inverters was affected by the voltage difference of the power sources.
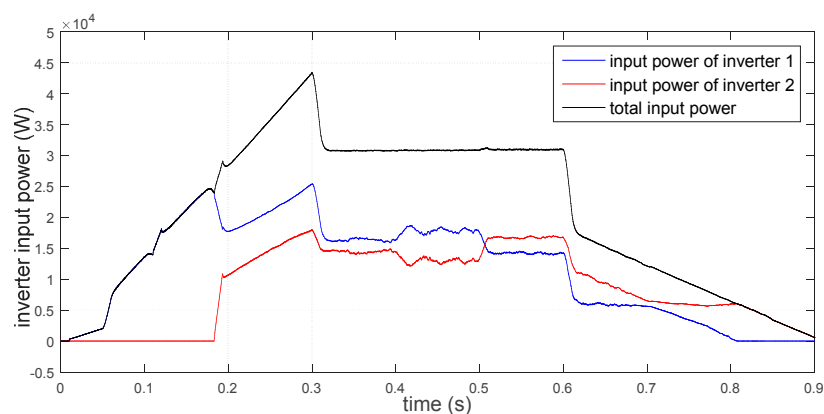

Figure 10. Curves of input power of both inverters.

An efficiency MAP of the drive system with switched winding modes and multi-level current hysteresis modulation is shown in Figure 11a; that of the contrasting drive system is shown in Figure 11b.
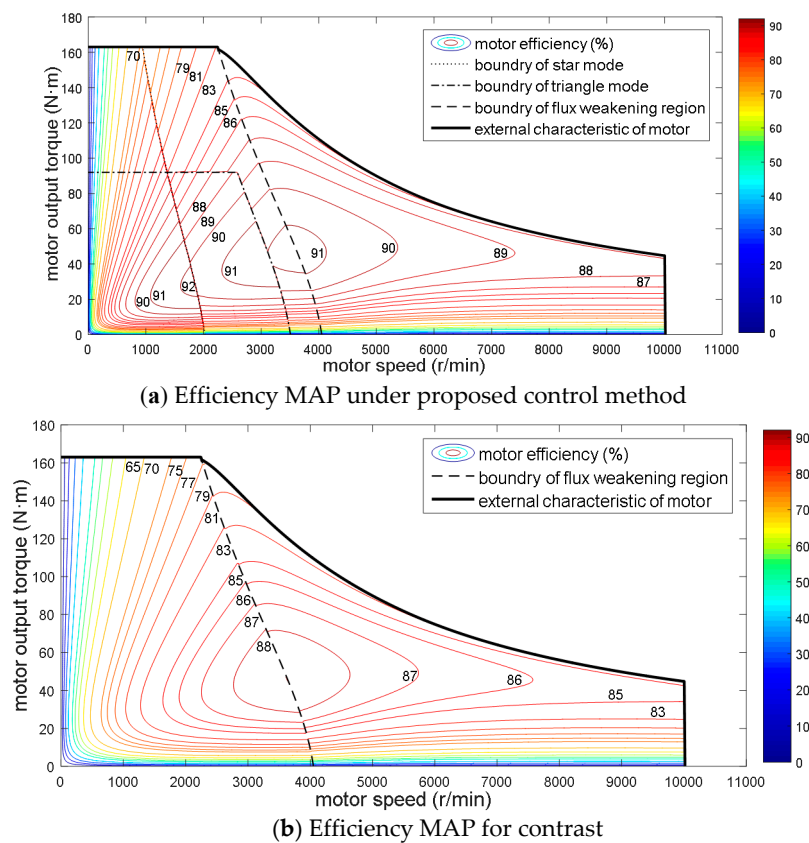
(**a**) Efficiency MAP under proposed control method

(**b**) Efficiency MAP for contrast

Figure 11. Efficiency MAP of drive system.

It is clear that the peak efficiency of the drive system under the proposed multi-level current hysteresis modulation is 3% higher than that of the contrasting drive system, because multi-level current hysteresis modulation reaches a lower switching frequency of inverter devices and then reduces inverter switching loss. We could also see that the high-efficiency area of the drive system is larger than in the contrasting system, extending to low speed and low torque areas, because in the region of star mode and triangle mode there is only one inverter working and producing switching loss. The iron loss caused by the stator voltage vector in the unsteady state is less than that in independent mode because the stator voltage amplitude in star and triangle mode is lower.

We also conducted a simulation of a small electric vehicle for economic performance. The drive system under the proposed control method was equipped, and the drive system under the traditional two-level current hysteresis modulation without winding mode switching function was also used for contrast. The basic parameters of the vehicle are shown in Table 6.

Table 6. Parameters of vehicle.

Items	Parameters
Vehicle weight m_0/kg	950
Drag coefficient C_d	0.30
Windward area A/m^2	2.11
Reduction gear ratio i_0	8.4
Rolling radius r_g/m	0.307
Rotational mass conversion factor δ	1.1
Rolling resistance coefficient f	0.015
Transmission efficiency η_m	0.95
Rate of braking energy regeneration R_b	0.6

We simulated four different type of driving cycles, NEDC (New European Driving Cycle), UDDS (Urban Dynamometer Driving Schedule), JC08 (Made by Japanese 2005 emission regulation), and HWFET (Highway Fuel Economy Test Cycle), representing a standard driving situation, an urban driving situation, a frequent acceleration and deceleration situation, and a highway driving situation respectively. The motor operating point distributions of the different driving cycles are shown in Figure 12.
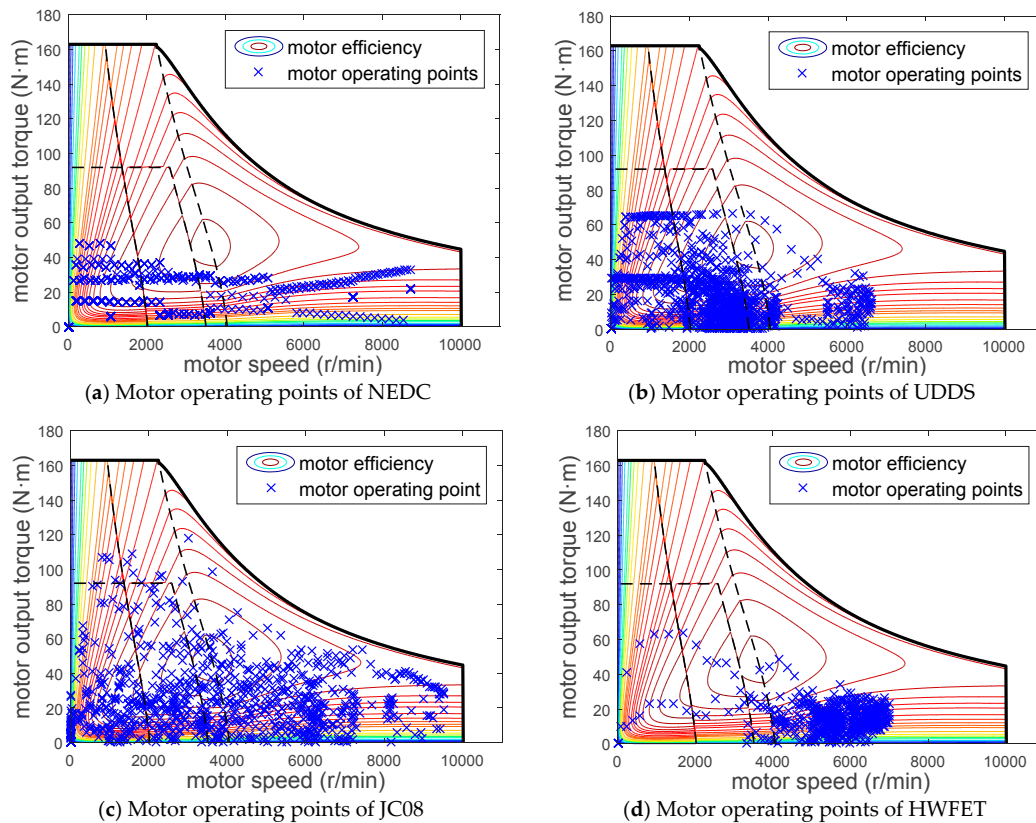

(**a**) Motor operating points of NEDC

(**b**) Motor operating points of UDDS

(**c**) Motor operating points of JC08

(**d**) Motor operating points of HWFET

Figure 12. Motor operating points in four driving cycles.

The efficiency distribution and power consumption of the proposed drive system and the contrasting drive system are shown in Table 7. The average efficiency distributions of the four driving cycles are shown in Figure 13.

Table 7. Efficiency distribution and power consumption.

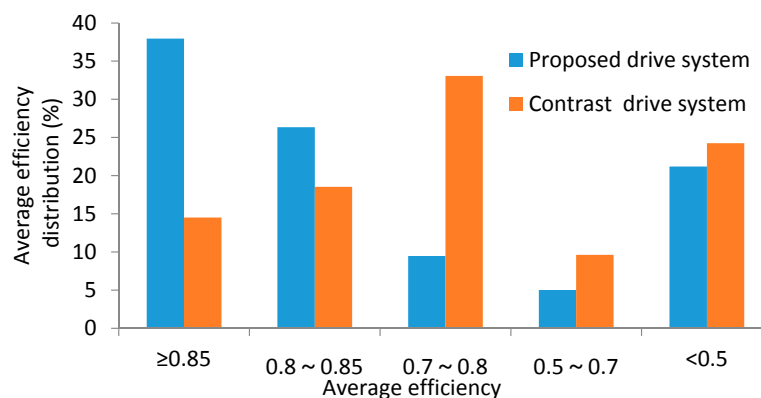| Driving Cycles		Efficiency Distribution/%					Power Consumption/ kWh 100 km^{-1}
		$\geq$0.85	0.8–0.85	0.7–0.8	0.5–0.7	<0.5	
Proposed drive system	NEDC	32.55	38.20	2.57	2.11	24.57	11.33
	UDDS	44.21	14.97	9.71	7.08	24.02	10.26
	JC08	46.62	9.71	6.31	5.52	31.84	15.17
	HWFET	28.41	42.52	19.33	5.36	4.38	12.52
	Average	37.95	26.35	9.48	5.02	21.20	12.32
Contrast drive system	NEDC	9.79	12.92	43.18	8.15	25.96	12.18
	UDDS	17.49	19.75	22.86	10.37	29.54	11.17
	JC08	24.66	17.14	13.74	9.55	34.91	16.23
	HWFET	6.14	24.30	52.51	10.45	6.60	13.27
	Average	14.52	18.53	33.07	9.63	24.25	13.21

Figure 13. Average efficiency distribution of four driving cycles.

It is evident that the proportion of high-efficiency working points of the proposed drive system is larger than that of the contrasting system, thus the power consumption is on average 6.75% lower than that of the contrasting system.

5. Conclusions

This paper, aimed at an electric vehicle equipped with an OW-PMSM drive system with dual power sources and dual inverters; based on analyzing the external characteristics of each winding mode, we produced a winding mode switching strategy whose torque saturation judgmental algorithm, insensitive to a motor's parameters, could automatically realize upswitching of winding mode. The proposed multi-level current hysteresis modulation algorithm can set the major power source and switch it at any time in independent mode, accomplishing energy distribution between two power sources; its two control methods, the low switching frequency method and the high power difference method, could achieve different energy distribution effects. From the simulation results, compared with an OW-PMSM drive system with traditional two-level current hysteresis modulation, under the same conditions the proposed system has 30% lower torque ripple and a lower switching frequency of inverter devices. Thus the proposed system has 3% higher peak efficiency and a larger high-efficiency area than a traditional OW-PMSM system. By applying it to electric vehicles, the power consumption is 6.75% lower on average under the proposed control methods. Moreover, through its two different control methods in independent mode, energy distribution between the two power sources can be realized, thus the DC/DC converter between them can be cancelled.

Finally, the proposed winding mode switching strategy and multi-level current hysteresis modulation method take full advantage of each winding mode's working range, reduce inverter switching loss, increase system efficiency, and realize energy distribution between two power sources. It provides a theoretical basis and implementation scheme a for dual-power OW-PMSM drive system in electric vehicles. Future research will be directed towards finding an energy distribution method matched with this system for electric vehicles to maximize the overall efficiency and driving range. After solving the existing practical issues, an experimental verification of the proposed system will also be conducted in an electric vehicle.

Author Contributions: Nan Xu and Liang Chu conceived the control method and revised the full manuscript; Yi-fan Jia and Dong-sheng Chen performed the simulation and wrote the full manuscript; Yan-wei Wang and Xin Tang analyzed the data; Zhe Xu analyzed and evaluated the simulation results and gave valuable suggestions.

Conflicts of Interest: The authors declare no conflict of interest.

References

1.   Chowdhury, S.; Wheeler, P.; Patel, C.; Gerada, C. A multilevel converter with a floating bridge for open-ended winding motor drive applications. *IEEE Trans. Ind. Electron.* **2016**, *63*, 5366–5375. [CrossRef]
2.   Loncarski, J.; Leijon, M.; Srndovic, M.; Rossi, C.; Grandi, G. Comparison of output current ripple in single and dual three-phase inverters for electric vehicle motor drives. *Energies* **2015**, *8*, 3832–3848. [CrossRef]
3.   Welchko, B.A.; Nagashima, J.M. A comparative evaluation of motor drive topologies for low-voltage, high-power EV/HEV propulsion systems. In Proceedings of the IEEE International Symposium on Industrial Electronics, Rio De Janeiro, Brazil, 9–11 June 2003; pp. 379–384.
4.   An, Q.T.; Duan, M.H.; Sun, L.; Wang, G.L. SVPWM strategy of post-fault reconfigured dual inverter in open-end winding motor drive systems. *Electron. Lett.* **2014**, *50*, 1238–1240. [CrossRef]
5.   Engelmann, G.; Kowal, M.; De Doncker, R.W. A highly integrated drive inverter using direct FETs and ceramic dc-link capacitors for open-end winding machines in electric vehicles. In Proceedings of the Applied Power Electronics Conference and Exposition, Charlotte, NC, USA, 15–19 March 2015; pp. 290–296.
6.   Sandulescu, P.; Meinguet, F.; Kestelyn, X.; Semail, E.; Bruyere, E. Control strategies for open-end winding drives operating in the flux-weakening region. *Power Electron. IEEE Trans.* **2014**, *29*, 4829–4842. [CrossRef]
7.   An, Q.; Liu, J.; Peng, Z.; Sun, L.; Sun, L. Dual-space vector control of open-end winding permanent magnet synchronous motor drive fed by dual inverter. *IEEE Trans. Power Electron.* **2016**, *31*, 8329–8342. [CrossRef]
8.   An, Q.; Sun, L.; Sun, L. Research on novel open-end winding permanent magnet synchronous motor vector control systems. *Proc. CSEE* **2015**, *22*, 5891–5898.
9.   Park, J.S.; Nam, K. Dual inverter strategy for high speed operation of HEV permanent magnet synchronous motor. In Proceedings of the Industry Applications Conference 2006, Ias Meeting, Tampa, FL, USA, 8–12 October 2006; pp. 488–494.
10. Kwak, M.S.; Sul, S.K. Flux weakening control of an open winding machine with isolated dual inverters. In Proceedings of the Industry Applications Conference 2007, Ias Meeting, New Orleans, LA, USA, 23–27 September 2007; pp. 251–255.
11. Rossi, C.; Grandi, G.; Corbelli, P.; Casadei, D. Generation system for series hybrid powertrain based on the dual two-level inverter. In Proceedings of the European Power Electronic Conferences, Barcelona, Spain, 8–10 September 2009; pp. 1–10.
12. Griva, G.; Oleschuk, V.; Profumo, F. Hybrid traction drive with symmetrical split-phase motor controlled by synchronized PWM. In Proceedings of the International Symposium on Power Electronics, Electrical Drives, Automation and Motion, Ischia, Italy, 11–13 June 2008; pp. 1033–1037.
13. Deng, Q.; Wei, J.; Zhou, B.; Han, C.; Chen, C. Research on control strategies of open-winding permanent magnetic generator. In Proceedings of the International Conference on Electrical Machines and Systems, Beijing, China, 20–23 August 2011; pp. 1–6.
14. Lee, Y.; Ha, J.I. Hybrid modulation of dual inverter for open-end permanent magnet synchronous motor. *IEEE Trans. Power Electron.* **2015**, *30*, 3286–3299. [CrossRef]
15. Casadei, D.; Grandi, G.; Lega, A.; Rossi, C. Multilevel operation and input power balancing for a dual two-level inverter with insulated DC sources. *IEEE Trans. Ind. Appl.* **2008**, *44*, 1815–1824. [CrossRef]
16. Welchko, B.A. A double-ended inverter system for the combined propulsion and energy management functions in hybrid vehicles with energy storage. In Proceedings of the Industrial Electronics Society 2005, IECON 2005, Raleigh, NC, USA, 6–10 November 2005.
17. Nipp, E. Permanent Magnet Motor Drives With Switched Stator Windings. Ph.D. Thesis, Royal Institute of Techonology, Stockholm, Sweden, May 1999.
18. Nguyen, N.K.; Semail, E.; Meinguet, F.; Sandulescu, P.; Kestelyn, X.; Aslan, B. Different virtual stator winding configurations of open-end winding five-phase PM machines for wide speed range without flux weakening operation. In Proceedings of the European Conference on Power Electronics and Applications, Lille, France, 2–6 September 2013; pp. 1–8.
19. Welchko, B.; Nagashima, J.M. The influence of topology selection on the design of EV/HEV propulsion systems. *IEEE Power Electron. Lett.* **2003**, *99*, 36–40. [CrossRef]
20. Nguyen, N.; Meinguet, F.; Semail, E.; Kestelyn, X. Fault-tolerant operation of an open-end winding five-phase PMSM drive with short-circuit inverter fault. *IEEE Trans. Ind. Electron.* **2014**, *63*, 595–605. [CrossRef]

21. Gu, C.; Zhao, W.; Zhang, B. Simplified minimum copper loss remedial control of a five-phase fault-tolerant permanent-magnet vernier machine under short-circuit fault. *Energies* **2016**, *9*, 860. [CrossRef]
22. Zhao, J.; Gao, X.; Li, B.; Liu, X.; Guan, X. Open-phase fault tolerance techniques of five-phase dual-rotor permanent magnet synchronous motor. *Energies* **2015**, *8*, 12810–12838. [CrossRef]
23. Zhan, H.; Zhu, Z.Q.; Odavic, M.; Li, Y.X. A novel zero sequence model based sensorless method for open-winding PMSM with common DC bus. *IEEE Trans. Ind. Electron.* **2016**, *63*, 6777–6789. [CrossRef]
24. Heng, N.; Zeng, H.; Zhou, Y. Zero sequence current suppression strategy for open winding permanent magnet synchronous motor with common DC bus. *Trans. China Electrotech. Soc.* **2015**, *30*, 40–48.
25. Sun, T.; Wang, J.; Chen, X. Maximum torque per ampere (MTPA) control for interior permanent magnet synchronous machine drives based on virtual signal injection. *IEEE Trans. Power Electron.* **2015**, *30*, 5036–5045. [CrossRef]
26. Zhang, Y.; Cao, W.; Mcloone, S.; Morrow, J. Design and flux-weakening control of an interior permanent magnet synchronous motor for electric vehicles. *IEEE Trans. Appl. Supercond.* **2016**, *26*, 1–6. [CrossRef]